HHS Public Access

Author manuscript

Adv Mater. Author manuscript; available in PMC 2021 April 23.

Published in final edited form as:

Adv Mater. 2019 August ; 31(33): e1901345. doi:10.1002/adma.201901345.

Additive Manufacturing of 3D Architected Multifunctional Metal Oxides

Daryl W. Yee[†,*], **Max L. Lifson**[†], **Bryce W. Edwards**, **Julia R. Greer [Prof.]**

Division of Engineering and Applied Science, California Institute of Technology, CA 91125, USA

Abstract

Additive manufacturing (AM) of complex three-dimensional (3D) metal oxides at the micro- and nano-scales has attracted considerable attention. State of the art techniques that use slurry-based or organic-inorganic photoresins are often hampered by challenges in resin preparation and synthesis, and/or by the limited resolution of patterned features. This study presents a facile process for fabricating 3D-architected metal oxides via the use of an aqueous metal-ion containing photoresin. The efficacy of this process, that we termed Photopolymer Complex Synthesis, is demonstrated by creating nano-architected zinc oxide (ZnO) architectures with feature sizes of 250 nm, by first patterning a zinc-ion containing aqueous photoresin using two-photon lithography and subsequently calcining them at 500°C. Transmission electron microscopy (TEM) analysis revealed their microstructure to be nanocrystalline ZnO, with grain sizes of 5.1 ± 1.6 nm. In-situ compression experiments conducted in a scanning electron microscope showed an emergent electromechanical response: a 200 nm mechanical compression of an architected ZnO structure resulted in a voltage drop of 0.52 mV. This photopolymer complex synthesis provides a pathway to easily create arbitrarily shaped 3D metal oxides that could enable previously impossible devices and smart materials.

Graphical Abstract

Fabrication of 3D nano-architected multifunctional metal oxides is achieved by a facile method using a metal-ion containing aqueous photoresin, which is then polymerized using two-photon lithography and finally calcined to give the metal oxide structure. Zinc oxide microstructures, with submicron features, fabricated using this technique exhibited an electromechanical response, which could enable the production of previously impossible 3D smart devices.

[*] daryl@caltech.edu.

[†]These authors contributed equally to this work.

Author contributions: M.L.L., D.W.Y. and J.R.G conceived and designed the experiments; D.W.Y. developed the polymer chemistry and fabricated the microstructures using two-photon lithography; D.W.Y. and M.L.L. developed the heating profile and performed SEM analyses; D.W.Y performed the EDS data collection and analysis. M.L.L. performed the XRD and TEM analyses; M.L.L built the electromechanical set-up and performed and analyzed the in-situ open circuit voltage response measurements. B.W.E performed and analyzed the in-situ compression experiments.

Supporting Information

Supporting Information is available from the Wiley Online Library or from the author.

Competing interests: A provisional patent has been filed on this work.

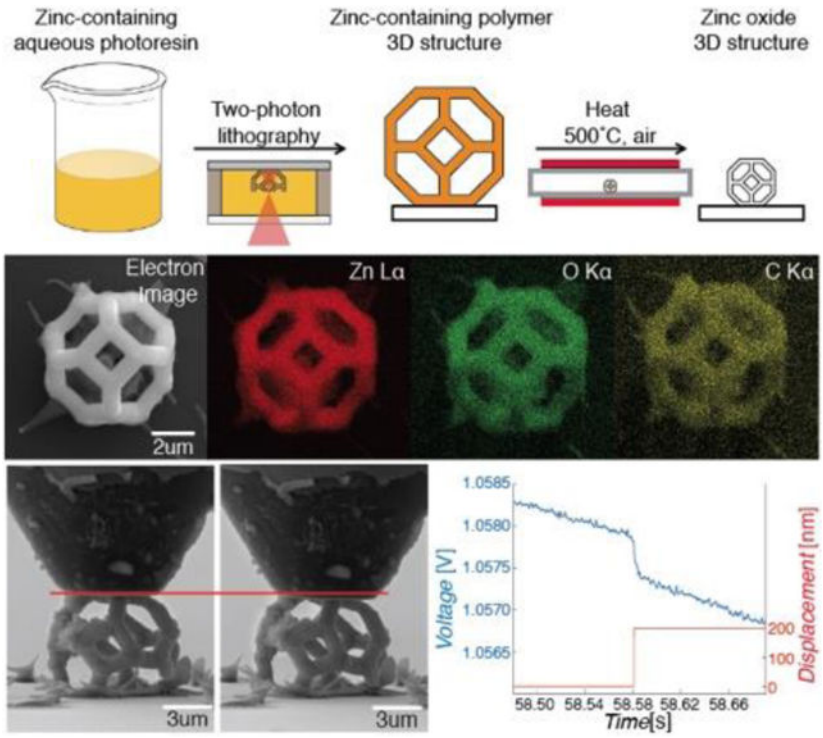

Keywords

Two-photon lithography; electromechanical; zinc oxide; metal oxide; 3D printing; Additive Manufacturing

Main Text

Multifunctional metal oxides represent an important class of materials used in modern society. These materials exhibit unique properties such as piezoelectricity,[1] superconductivity,[2] and semiconductivity,[3] rendering them useful in virtually every type of micro/nanosystem device technology. Most current device designs utilize metal oxides as thin film stacks because patterning these materials has mostly been achieved using traditional planar lithography, which substantially limits the geometries that can be achieved.[4] New experimental devices that utilize three-dimensional (3D) metal oxides demonstrate substantial improvements in performance:[5,6] for example, using a templated approach, Lu et al. fabricated 3D lithium cobalt oxide (LCO) cathodes that delivered an areal capacity of 22.7 mAh cm^{-2}, a value at least three times higher than that of typical commercial LCO cathodes.[7,8] In some cases, architecting a material enables previously unattainable functionalities: for example, hollow-tube 3D architected Al_2O_3 nanolattices recovered up to 98% of their original height after compression to >50% strain.[9] Multiple advanced fabrication techniques have been developed to create 3D architectures, with varying degrees of success. Bottom up approaches, in which micro/nanostructures are precipitated from solution in a controlled fashion, have largely been limited to simple shapes like tubes,[10] wires,[11] and cubes.[12] Top down methods that utilize lithography stacks,[13,14] templated

growth,[15] out-of-plane buckling,[16] and directed self-assembly[17] offer better capabilities in fabricating a larger range of complex 3D geometries, but either require multiple complicated processing steps or are limited in geometries and dimensions that can be achieved.

Additive manufacturing (AM) has recently emerged as a frontrunner for the fabrication of three-dimensional metal oxide structures with almost arbitrary geometries. A wide variety of AM techniques currently exist to 3D print metal oxides:[18–20] from laser-based processes like selective laser sintering[21,22], selective laser melting,[23–25] and photolithography,[26–28] to ink-based ones such as fused deposition modeling,[29,30] and inkjet printing.[31–34] All of these techniques are based on layer-by-layer fabrication, which allows for the construction of almost arbitrarily complex architectures. Processes that involve photolithography are able to achieve feature resolutions from several microns to below 100nm,[35] which makes them useful for micro-electro-mechanical systems (MEMS). One common approach that utilizes photolithography is to use a photosensitive slurry, where a high volume fraction of metal oxide powder is dispersed in a photoresin. The slurry is patterned using micro-stereolithography to create 3D nanocomposite structures, which are then calcined to burn off the organic matrix and to sinter the metal oxide particles together.[36,37] Using this approach, Dufaud et al. patterned a photosensitive slurry of lead zirconate titanate (PZT) powder using stereolithography to produce PZT nanocomposite structures, and then calcined them at 900°C to produce PZT replicas with <300 μm resolution.[38] Applying the same technique to a photoresin filled with SiO_2 nanoparticles instead, Kotz et al. were able to fabricate transparent fused silica glass structures with a minimum feature size of 80 μm.[39] A major drawback of this methodology is that the high loading of particles in the resin induces a significant light-scattering effect, which prevents the lithography techniques from achieving the <20 μm resolution that can be achieved with conventional transparent photoresins.[40–42] This light-scattering also renders them incompatible with other high resolution photolithography techniques like two-photon lithography (TPL).[43] To circumvent this problem and achieve sub-micron resolution, nanoparticle-less organic-inorganic photoresists have been developed. These photoresists typically contain inorganic polymers that have metal heteroatoms in their backbone[44,45] or have small metal complexes dispersed in an organic medium.[46] For example, Gailevičius et al. synthesized a silicon and zirconia sol-gel photoresist, patterned it using TPL, and then calcined it at 1500°C to obtain 3D polycrystalline structures of SiO_2 and ZrO_2 with 100 nm feature sizes.[35] Using a similar approach, Passinger et al. developed a photosensitive sol-gel-based spin-coatable TiO_2 resist, which could be used with TPL to directly obtain TiO_2 3D structures with sub-micron resolution.[47] A key disadvantage of this approach is that these photoresists are often not commercially available and sometimes require a complex multi-step synthesis. To fabricate arbitrarily shaped 3D metal oxide microstructures, a process that combines the beneficial aspects of existing approaches: (1) the simplicity and versatility of the slurry method and (2) the high resolution afforded by the organic-inorganic photoresists, has to be developed.

We developed a simple and efficient synthesis route whereby aqueous metal-ion containing photoresins are used with stereolithography techniques to produce metal-ion containing 3D polymer architectures that are subsequently converted into their metal oxide replicas via calcination. To demonstrate the feasibility and efficiency of this technique, we prepared a

zinc-ion containing photoresin and used it with TPL to produce 3D zinc oxide (ZnO) architectures with sub-micron features. We chose ZnO as a model material because it has a suite of useful properties, such as a direct band gap and piezoelectricity.[48] Attempts to fabricate this material in 3D have included extrusion,[49] templated approaches,[50,51] core-shell composites,[52,53] and nanocomposites,[54] all of which have been unable to fabricate monolithic ZnO 3D microstructures with both arbitrary design and high resolution. Our slurry-free, photolithography method to create monolithic three-dimensional ZnO structures represents a significant simplification from the state of the art and enables previously impossible architectures and device designs.

To prepare the resin, we first dissolved zinc nitrate hexahydrate in water and then mixed it with poly(ethylene glycol) diacrylate (PEGda). A two-photon initiator, 7-diethylamino-3-thenoylcourmarin (DETC) was then dissolved in dimethyl sulfoxide (DMSO) and added to the zinc-PEGda solution, which yielded a pale homogenous orange solution. The composition of the resin was ~51 wt% zinc nitrate hexahydrate and 0.08 wt% DETC. These compositions were determined using an iterative approach where the goal was to maximize the amount of zinc nitrate hexahydrate and DETC in the resin, while still maintaining homogeneity and long-term stability of the photoresin. The photoresin was drop-cast onto a silicon substrate and patterned using TPL (more details on the TPL set up, resolution achievable, and the writing parameters (Figure S2) can be found in the Supporting Information) to directly fabricate the desired cross-linked zinc-ion containing 3D polymer structures. These structures were then developed in water and subsequently calcined at 500 °C to obtain their corresponding ZnO architectures. 500°C was chosen as the calcination temperature based on thermogravimetric analysis (TGA) of these zinc-containing polymers (Figure S4), which demonstrated that this temperature was sufficiently high for the complete conversion of the zinc nitrate hexahydrate into zinc oxide and for the removal of all other organics. We used a conservative heating ramp rate of 0.5 °C/min to minimize the amount of violent outgassing of volatiles during the calcination process. A step-by-step schematic of this process is demonstrated in Figure 1.

We found the linear shrinkage after calcination to depend on the initial concentration of metal salt in the resin and on the development time of the printed structure in water. A simple analytical model based on the conversion of all zinc nitrate hexahydrate into zinc oxide, predicted the theoretical minimum linear shrinkage using this photoresin to be ~67%. During the development process, the zinc ions are able to leach out of the polymer and diffuse into the water, which reduces the amount of zinc nitrate left in the polymer and consequently, the final volume of the zinc oxide architecture after calcination. Figure S3 shows the dependence of development time on the final linear shrinkages as measured by fabricating cylinders 15 μm in height and 9.5 μm in diameter, systematically varying their development time in water and measuring their dimensions before and after calcination. It showed that for the shortest development time of 1 min, the observed shrinkage of ~70% was in good agreement with the 67% determined by the proposed analytical model. Linear shrinkages increased for longer development times, attaining the smallest beam diameter of 0.9 nm, which represents a ~90% post-calcination dimensional change and supports the mechanism of zinc ions being leached into the water over time. Analysis of the radial and axial shrinkages also indicated the shrinkages to be isotropic, with the absolute difference

between the two shrinkage measurements being <2%. This method of tuning the linear shrinkage obtained after calcination via leaching of zinc ions effectively provides another mechanism for refining the resolution of the structures printed using this technique.

To demonstrate the high resolutions achievable with this technique, we created architectures of increasing complexity using two-photon lithography: from cylindrical pillars to individual unit cells to microlattices, and developed them in water for five minutes, followed by calcination at 500°C. Figure 2 contains side-by-side scanning electron images (SEM) of these architectures before (polymeric) and after (metal oxide) calcination: a cylindrical pillar (Figure 2a), a tetrakaidecahedron unit cell (Figure 2b) and a microlattice of tetrakaidecahedrons (2 × 2 × 2 unit cells) (Figure 2c), all of which appear to have fully resolved features with uniform beams. Each structure was fabricated on top of a pre-designed support to prevent the generation of interfacial stress between the sample and the substrate caused by their dissimilar rates of shrinkage during calcination. The support geometry is not unique and can be as simple as a pedestal (Figure 2b) or as complicated as a layer of tetrakaidecahedron unit cells (Figure 2c). After calcination, the supports were largely destroyed and self-similar ZnO architectures with each dimension reduced by ~87 ± 2 % remained. The intrinsic high resolution of the structures fabricated using TPL combined with the substantial linear shrinkage allowed for the production of complex 3D structures with feature resolution on the order of 250 nm. Table S1 summarizes the linear shrinkage measurements of these structures and calculation according to Equation S2.

The concept of entrapping metal ions within a polymer network prior to calcination has been exploited in metal oxide nanoparticle synthesis methods like the Pechini process, and the polymer complex solution (PCS) method.[55] The lack of spatial control over the polymer network formation in those techniques precluded them from being able to fabricate more complex micro/nanostructures. Our developed methodology achieves spatial control of the polymerization process via the use of telechelic PEGda macromonomers and a suitable photoinitiator. The conversion process from polymer to metal oxide is a strong function of temperature and of the chemistry and concentration of the metal salt precursor. For example, in the solution combustion synthesis (SCS) and PCS methods, strongly oxidizing metal nitrates are mixed with water-soluble chelating organic molecules and then heated until a rapid combustion occurs. The released heat is sufficient to volatize the organic binder molecules and form metal oxide nanoparticles.[56,57] Figure S4 shows the TGA data of a zinc-nitrate containing polymer and of a PEGda control polymer made using this technique, that contained an equivalent volume of water instead of the zinc nitrate solution. The plot revealed that the zinc-nitrate containing polymer first exhibited a mass change of ~16 wt% as it approached 115°C, likely from the loss of bound water in the polymer, followed by a rapid mass loss of ~50 wt% from 115 – 150°C. This rapid change of mass over a small temperature window is characteristic of SCS and has been observed in combustion synthesis studies with zinc nitrate.[58] Further heating to 400°C showed an additional mass loss of ~16 wt%, with a negligible mass change at higher temperatures. The control polymer showed a mass loss of ~50 wt% up to 100°C, which can be attributed to water loss. The polymer then underwent a gradual mass loss of ~40 wt% on subsequent heating from 170 to 400°C, and completely degraded past 500°C. This distinct difference in the TGA signature provides evidence that the zinc nitrate precursor initiates a combustion process during calcination.

This process of 3D printing metal-nitrate polymers that undergo combustion during heat treatment inspired us to coin this process “Photopolymer Complex Synthesis”, a portmanteau of photolithography, polymer complex solution, and solution combustion synthesis – the three fields from which this methodology draws.

We used a suite of techniques to characterize the calcined materials. After calcination, the zinc-ion containing and control samples were heated to 500°C in air at a rate of 0.5 °C/min and then immediately cooled to room temperature at a rate of 2 °C/min. The resulting materials were an off-white brittle ceramic (zinc-ion containing sample) and grey ash (control PEGda photopolymer), which is consistent with both ZnO and carbon residue, respectively. Figure 3a contains X-ray diffraction (XRD) spectra of both calcined samples that were initially prepared by casting the photoresins into centimeter-sized molds and photopolymerizing them with UV light instead of TPL because the sample size requirements for the XRD exceed those that are practical with TPL. These spectra clearly reveal that the sample made with the zinc nitrate precursor has sharp diffraction peaks that are in good agreement with those of ZnO (JCPDS card no. 36–1451) and did not contain any discernible impurities, such as zinc carbonate. The XRD spectrum of the control sample had a single broad peak at low angles, which implies that the sample likely only contained amorphous carbon.

Figure 3b shows the Energy-dispersive X-ray spectroscopy (EDS) elemental maps of a tetrakaidecahedron unit cell fabricated via two-photon lithography and then subsequently calcined. A homogenous distribution of zinc, oxygen and carbon can be clearly seen throughout the solid, with no apparent segregation into individual element-rich phases. EDS analysis in Figure 3c revealed that the atomic percentages of Zn and O, after excluding silicon from the substrate and carbon from various sources, were 45.0 and 48.9 at% respectively, resulting in a Zn to O ratio of 0.92. This composition should be treated as an approximation due to the inaccuracies associated with measuring light elements using EDS. Carbon was excluded from our analysis due to the unknown contributions of the carbon signal from both the structure and the substrate (Figure S5). Possible sources of C on the substrate include combustion residue and SEM chamber deposits.[59]

Bright field (Figure 3d), dark field (Figure 3e), and high-resolution (Figure 3g) Transmission Electron Microscopy (TEM) images of a typical beam cross-section (Figure S6), reveal that the calcined ZnO is fully dense (i.e. not porous) and nanocrystalline, with a mean grain size of 5.1nm ± 1.6 nm (N=40). The selected area electron diffraction (SAED) pattern (Figure 3h) contains characteristic rings, whose spacing corresponds to the labeled crystallographic orientations of polycrystalline ZnO. The outermost ring is labeled (112) / (201) because the spacing of these two orientations was so close that it was not possible to distinguish between them experimentally. The two large diffraction spots in the lower left quadrant of the diffraction pattern are likely a result of electron beam overlap with the underlying silicon substrate. These three independent characterization techniques strongly suggest that calcination of the zinc-ion containing polymer structures at 500°C resulted in its conversion to monolithic polycrystalline ZnO.

To demonstrate the potential of these architected ZnO microstructures as electromechanical device elements, we designed and custom-built an electromechanical experimental setup to simultaneously probe these 3D ZnO structures mechanically and electrically in an in-situ nanomechanical instrument inside of an SEM chamber (Figure S7).

Using this methodology, we measured the open circuit voltage (OCV) during in-situ compressions of a tetrakaidecahedron ZnO structure and a similar control structure made of the zinc-ion containing polymer (Figure 4). Printing parameters, size, and design of the ZnO and polymer structures were nominally identical, which resulted in the poorly resolved polymer structure due to the inability of TPL alone to reach the resolution afforded by the combination of TPL and calcination. OCV measurements during in-situ compression of the polymer tetrakaidecahedron (Figure 4b and 4c) showed no deviation from the long-term transient response of the measurement system, which resembles the exponential decay of a discharging capacitor (Figure S9). This can be attributed to the experimental set-up, where the applied displacement was obtained by careful image analysis before and after each incremental displacement of the nanoindenter tip. This imaging likely resulted in the build up of charge in the non-conductive samples, which then dissipated through the complex circuit over the long time constant of the system during OCV measurement. For the short time frames involved with each experiment, this background response appears linear. These results indicate that the zinc-ion containing polymer did not exhibit any electrical response upon compression. An analogous in-situ compression of the ZnO tetrakaidecahedron (Figure 4f and Figure 4g) revealed a distinct voltage drop of 0.52 mV in response to a displacement of 200 nm (~2.5% compressive strain) at t = 58.58 seconds. This difference between the two tests clearly highlights the electromechanical coupling in the ZnO structures and a lack thereof in the zinc-containing polymer control, and indicates that full conversion of the zinc-containing polymer to zinc oxide is necessary to elicit an electromechanical response. OCV measurements did not short upon contact with the ZnO sample, which indicates that the carbon observed in Figure 3b did not form an electrically conductive pathway. Cyclic compression experiments on an individual ZnO tetrakaidecahedron unit cell, using a separate commercial in-situ compression set-up, demonstrated the mechanical resilience of these 3D ZnO architectures. Complete shape recovery was observed after 9 cycles of uniaxial compressions of 200 nm, with no signs of catastrophic or localized failure (Figure 4i–k). The loading and unloading stiffness of the structure for the 9 compression cycles were determined to be 2.37 ± 0.15 kN/m and 2.52 ± 0.13 kN/m, and did not exhibit any discernible trends over the course of the experiment. The slight displacement shifts observed in the data were likely due to drift within the mechanical experiment. The compressive strain to failure for these structures was approximately 3.5%, which was expected since ZnO is a brittle ceramic. The potential mechanical degradation of these structures over time is a subject of a future study. Further information on this OCV experimental procedure, expected equivalent circuit (Figure S10), mechanical properties (Figure S11 and S12), and compression videos can be found in the Supporting Information.

There are numerous potential applications of these nano-architected electromechanical ZnO structures as devices – the voltage output of these structures are in the usable range to switch low voltage logic relays.[60] For example, Zaghloul et al. fabricated a nanoelectromechanical system (NEMS) switch with a threshold voltage of 0.2 mV,[61] which is well within the

voltages generated from the ZnO structures in this work. A step-up convertor can also be used to amplify the generated voltages from tens of millivolts to single digit volts, for a variety of energy harvesting, logic, and transducer applications.[62] Existing studies on 3D printing ZnO have largely focused on its other functional properties, such as its ability to be used as a desulfurization agent,[63] or as a UV photodetector.[34] We believe that this work constitutes the first demonstration of an electromechanical response from a 3D printed monolithic ZnO structure. The ability to 3D print ZnO into a variety of different shapes will enable control and tailoring of the electromechanical response, due to the influence that sample geometry has on the strain landscape within the solid, as evidenced by recent studies on the impact of geometry on the piezoelectric response of other piezoelectric materials.[64,65] The quantification and mechanism of this electromechanical response of the nanocrystalline ZnO microstructures using this custom measurement system, the mechanism and impact of the microstructure produced from this fabrication method, and the effect of geometrical features on the electrical response all merit their own independent investigations and are subjects of a future in-depth study.

We developed a simple method to fabricate 3D architected metal oxides via photopolymer complex synthesis. As a proof of concept, we fabricated 3D nano-architected ZnO into increasingly complex shapes, from pillars, to tetrakaidecahedron lattices to highlight its versatility in fabricating complex architectures that could be used as electromechanical devices. In contrast to the current state-of-the-art slurry and sol-gel photoresin approaches, our aqueous metal-ion containing photoresins provide a simple and inexpensive route for fabricating monolithic 3D structures of arbitrarily complex geometries with feature sizes below 1 um. The demonstrated capability to fabricate nano-architected three-dimensional ZnO shapes with feature sizes of the order of 250 nm is a significant step forward from the state of the art and could finally allow for the realization of currently inaccessible 3D piezoelectric microstructures. This technique can easily be translated to other metal oxides: any water-soluble metal salt can be used in the preparation of the photoresin, shaped with an appropriate photolithography technique, and then calcined to make its corresponding metal oxide. The versatility of photopolymer complex synthesis in fabricating 3D multifunctional metal oxides has direct implications in a variety of fields, from nano-electromechanical systems to chemical catalysis, energy storage, and new material synthesis, and could enable the production of previously impossible 3D smart devices.

Experimental Section

Materials:

Zinc nitrate hexahydrate (98%, Sigma-Aldrich), poly (ethylene glycol) diacrylate M_n = 575 (PEGda 575) (Sigma-Aldrich), 7-diethylamino-3-thenoylcoumarin (DETC) (Exciton), lithium phenyl-2,4,6-trimethylbenzoylphosphinate (LAP) (>95%, Sigma-Aldrich) and dimethyl sulfoxide (DMSO) (Sigma-Aldrich) were used as received without further purification.

Zinc-ion containing aqueous photoresin for two-photon lithography (Z1):

To prepare the zinc-ion containing aqueous photoresin, 5g of zinc nitrate hexahydrate was first dissolved in 1 mL of deionized water to give a solution of volume 3.6 mL. To the zinc nitrate solution, 2.67 mL of PEGda 575 was added and mixed until a homogenous transparent solution was formed. In a separate vial, 6.2 mg of the two-photon initiator DETC was dissolved in 465 μL of DMSO to give a yellow solution. 500 μL of the zinc nitrate/ PEGda solution was then mixed with 50 μL of the DETC solution to give a pale orange solution.

Zinc-ion containing aqueous photoresin for x-ray diffraction and thermogravimetric analysis characterization (Z2):

To prepare the zinc-ion containing aqueous photoresin, 5g of zinc nitrate hexahydrate (Sigma-Aldrich) was first dissolved in 1 mL of deionized water to give a solution of volume 3.6 mL. To the zinc nitrate solution, 2.67 mL of PEGda 575 was added and mixed until a homogenous colorless transparent solution was formed. In a separate vial, 23 mg of the photoinitiator LAP was dissolved in 1 mL of deionized water to give a colorless transparent solution. 2 mL of the zinc nitrate/ PEGda solution was then mixed with 50 μL of the LAP solution to give a colorless transparent solution.

Control aqueous photoresin for x-ray diffraction and thermogravimetric analysis characterization (C1):

To prepare the control aqueous photoresin, 3.6 mL of deionized water was added to 2.67 mL of PEGda 575 to give a clear solution. In a separate vial, 23 mg of LAP was dissolved in 1 mL of deionized water. 50 μL of the LAP solution was then added to 2 mL of water/ PEGda 575 and mixed until a homogenous colorless transparent solution was formed.

Additive manufacturing via two-photon lithography:

Two-photon lithography was performed using a commercially available system (Photonic Professional GT, Nanoscribe GmbH) using a Zeiss Plan-Apochromat 63x/1.4 Oil DIC objective. Rastering of the laser was achieved via a set of galvo-mirrors and piezoelectric actuators. For all the structures made, the laser power and scan speed were set at 50 mW and 1 mm s^{-1} respectively. Glass substrates 30 mm in diameter and 0.17 mm thick were used in conjunction with silicon chips 1 cm (L) x 1 cm (W). The zinc-ion containing aqueous photoresin Z1 was drop casted onto the glass substrate and then a silicon chip placed over it, using Kapton tape of approximately 100 μm in thickness as a spacer (Figure S1). The structures were then written on the silicon chip via two-photon lithography. The finished sample was developed in deionized water for 5 minutes.

Curing of photopolymers for x-ray diffraction and thermogravimetric analysis characterization:

1.5 mL of the aqueous photoresin (either Z2 or C1) was poured into a polydimethylsiloxane circular mold 4 cm in diameter and then cured with a UV curing lamp (350–380 nm, 36W) (MelodySusie DR 301C) for 60 minutes.

Calcination:

Samples were calcined in a furnace (MTI OTF-1500X) at ambient pressure in air at 0.5°C/min to 500°C and then cooled back to room temperature at 2°C/min.

Material Characterization (SEM, EDS, XRD, TGA):

Samples were imaged in an SEM (FEI Versa 3D) before and after calcination at 2kV.

Post-calcination EDS maps were generated in a Zeiss 1550VP FESEM equipped with an Oxford X-Max SDD EDS system. The applied voltage was 15 kV.

XRD (Bruker D2 Phaser) data was collected at 30kV and 10mA using a Cu source with a Lynxeye detector.

TGA was performed on a STA 6000 (PerkinElmer) from 30 to 900°C at a heating rate 5°C min^{-1} under air with a flow rate of 20 mL min^{-1}. Small samples of Z2 or C1 <100 mg were used for this analysis.

TEM liftout samples were created using traditional methods in a dual beam FIB (FEI Versa 3D) and micromanipulator (EZLift). An image of the liftout sample can be found in Figure S6. Gas-injected platinum was used to deposit a protection layer during the FIB process and gluing layers for moving the liftout sample and attaching it to a post on a half-moon copper TEM grid. Samples were then imaged in a TEM (FEI Tecnai F30) at 300kV. All sample measurements were performed in the microscope software (FEI) or via image software (ImageJ) after imaging.

Electromechanical Response In-Situ Experiments:

In-situ electrical measurements were performed in a modified SEM (FEI Quanta 200F) with an attached nanomechanical indenter arm (InSEM from Nanomechanics Inc.). A potentiostat (BioLogic SP200) was used to measure the open circuit voltage between the stage, which was held at ground, and the 4 um tungsten carbide flat punch tip (Synton-MDP Inc.) that made contact with the top of the sample. Discrete displacements of the flat punch tip into the sample were controlled directly through the linear motor controller (Zaber Technologies Inc.) of the indenter arm and the displacement was verified via SEM images. MATLAB code was created to identify and measure any deviations in the data from the typical observed signal decay in the timeframe of the mechanical displacement. A schematic of the experimental setup (Figure S7) and further details are described below in the supplementary text.

In-Situ Compression Experiments:

Samples were compressed using a 15 μm diamond flat punch (Synton-MDP Inc.) affixed to a nanoindenter (InSEM from Nanomechanics Inc.) installed in an SEM chamber (FEI Quanta 200F) that allowed for in-situ imaging of the sample during the compression test. The compressions were done at room temperature at a pressure of around 10^{-5} mbar at a displacement rate of 8 nm/s, which corresponded to a strain rate of approximately 10^{-3} s^{-1} for these unit cells. For the cyclic tests, a moving average filter was applied to the load-

displacement data to reduce noise and ease visualization of each cycle preformed. More details can be found in the Supporting Information.

Supplementary Material

Refer to Web version on PubMed Central for supplementary material.

Acknowledgements

M.L.L. and D.W.Y. contributed equally to this work. The authors would like to thank the following people: J. H. Kang and the Davis lab at Caltech for performing TGA analysis, M. T. Johnson and the Faber lab at Caltech for assistance with our preliminary thermal process, R. A. Gallivan for her assistance with the electromechanical experiments and thoughtful discussions. C. M. Garland for her assistance with TEM imaging and A. Vyatskikh for helpful discussions.

Funding: The authors gratefully acknowledge the financial support from the National Institutes of Health (Grant No. 1R01CA194533), the Gwangju Institute of Science and Technology (Grant No. CG2014), and the Department of Defence through JRG's Vannevar-Bush Fellowship. The authors would also like to acknowledge the support granted by the NIH Biotechnology Leadership Training Program (Grant No. T32GM112592) and the Donna and Benjamin M. Rosen Bioengineering Center at Caltech.

References

[1]. Bowen C, Kim H, Weaver P, Dunn S, Energy Environ. Sci 2014, 7, 25.

[2]. Cava RJ, J. Am. Ceram. Soc 2000, 83, 5.

[3]. Zhai T, Fang X, Liao M, Xu X, Zeng H, Yoshio B, Goldberg D, Sensors 2009, 9, 6504. [PubMed: 22454597]

[4]. Geissler M, Xia Y, Adv. Mater 2004, 16, 1249.

[5]. Sun K, Wei TS, Ahn BY, Seo JY, Dillon SJ, Lewis JA, Adv. Mater 2013, 25, 4539. [PubMed: 23776158]

[6]. Nistorica C, Latev D, Gardner D, Imai D, Daft C, in 2015 IEEE International Ultrasonics Symposium (IUS), IEEE, 2015, pp. 1–4.

[7]. Lu LL, Lu YY, Xiao ZJ, Zhang TW, Zhou F, Ma T, Ni Y, Yao HB, Yu SH, Cui Y, Adv. Mater 2018, 30, 1706745.

[8]. Lai W, Erdonmez CK, Marinis TF, Bjune CK, Dudney NJ, Xu F, Wartena R, Chiang YM, Adv. Mater 2010, 22, E139. [PubMed: 20301129]

[9]. Meza LR, Das S, Greer JR, Science 2014, 345, 1322. [PubMed: 25214624]

[10]. Zhang G, Xia BY, Xiao C, Yu L, Wang X, Xie Y, Lou XW, Angew. Chem 2013, 125, 8805; Angew. Chem. Int. Ed. 2013, 52, 8643.

[11]. Lifson ML, Levey CG, Gibson UJ, Appl. Phys. A 2013, 113, 243.

[12]. Fei JB, Cui Y, Yan XH, Qi W, Yang Y, Wang KW, He Q, Li JB, Adv. Mater 2008, 20, 452.

[13]. Shen D, Park JH, Ajitsaria J, Choe SY, Wikle III HC, Kim DJ, J. Micromechanics Microengineering 2008, 18, 055017.

[14]. Han Z, Salmi E, Vehkamäki M, Leskelä M, Ritala M, Nanotechnology 2018, 29, 055301.

[15]. Liu Z, Fan T, Zhang W, Zhang D, Microporous Mesoporous Mater. 2005, 85, 82.

[16]. Xu S, Yan Z, Jang KI, Huang W, Fu H, Kim J, Wei Z, Flavin M, McCracken J, Wang R, Badea A, Science 2015, 347, 154. [PubMed: 25574018]

[17]. Zheng W, Jacobs HO, Adv. Funct. Mater 2005, 15, 732.

[18]. Zhou X, Liu C. j., Adv. Funct. Mater 2017, 27, 1701134.

[19]. Ruiz-Morales JC, Tarancón A, Canales-Vázquez J, Méndez-Ramon J, Hernández-Afonso L, Acosta-Mora P, Rueda JM, Fernández-González R, Energy Environ. Sci 2017, 10, 846.

[20]. Cooperstein I, Sachyani-Keneth E, Shukren-Farrell E, Rosental T, Wang X, Kamyshny A, Magdassi S, Adv. Mater. Interfaces 2018, 5, 1800996.

[21]. Bertrand P, Bayle F, Combe C, Gœuriot P, Smurov I, Appl. Surf. Sci 2007, 254, 989.
[22]. Exner H, Horn M, Streek A, Ullmann F, Hartwig L, Regenfuß P, Ebert R, Virtual Phys. Prototyp 2008, 3, 3.
[23]. Wilkes J, Hagedorn Y-C, Meiners W, Wissenbach K, Rapid Prototyping J. 2013, 19, 51.
[24]. Yves-Christian H, Jan W, Wilhelm M, Konrad W, Reinhart P, Phys. Procedia 2010, 5, 587.
[25]. Pan H, Misra N, Ko SH, Grigoropoulos CP, Miller N, Haller EE, Dubon O, Appl. Phys. A 2009, 94, 111.
[26]. Wu H, Liu W, He R, Wu Z, Jiang Q, Song X, Chen Y, Cheng L, Wu S, Ceram. Int 2017, 43, 968.
[27]. Schwentenwein M, Homa J, Int. J. App. Ceram. Tech 2015, 12, 1.
[28]. Mitteramskogler G, Gmeiner R, Felzmann R, Gruber S, Hofstetter C, Stampfl J, Ebert J, Wachter W, Laubersheimer J, Addit. Manuf 2014, 1, 110.
[29]. Salea A, Prathumwan R, Junpha J, Subannajui K, J. Mater. Chem C 2017, 5, 4614.
[30]. Zhang J, Zhao S, Zhu M, Zhu Y, Zhang Y, Liu Z, Zhang C, J. Mater. Chem. B 2014, 2, 7583. [PubMed: 32261896]
[31]. Wang J, Shaw LL, J. Am. Ceram. Soc 2006, 89, 3285.
[32]. Saleh E, Woolliams P, Clarke B, Gregory A, Greedy S, Smartt C, Wildman R, Ashcroft I, Hague R, Dickens P, Tuck C, Addit. Manuf 2017, 13, 143.
[33]. Liu X, Tarn T-J, Huang F, Fan J, Particuology 2015, 19, 1.
[34]. Tran VT, Wei Y, Yang H, Zhan Z, Du H, Nanotechnology 2017, 28, 095204.
[35]. Gailevičius D, Padolskytė V, Mikoliūnaitė L, Šakirzanovas S, Juodkazis S, Malinauskas M, Nanoscale Horiz. 2019.
[36]. Zocca A, Colombo P, Gomes CM, Günster J, J. Am. Ceram. Soc 2015, 98, 1983.
[37]. Hinczewski C, Corbel S, Chartier T, J. Eur. Ceram. Soc 1998, 18, 583 (1998).
[38]. Dufaud O, Corbel S, Rapid Prototyping J 2002, 8, 83.
[39]. Kotz F, Arnold K, Bauer W, Schild D, Keller N, Sachsenheimer K, Nargang TM, Richter C, Helmer D, Rapp BE, Nature 2017, 544, 337. [PubMed: 28425999]
[40]. Halloran JW, Annu. Rev. Mater. Res 2016, 46, 19.
[41]. Layani M, Wang X, Magdassi S, Adv. Mater 2018, 30, 1706344.
[42]. Manapat JZ, Chen Q, Ye P, Advincula RC, Macromol. Mater. Eng 2017, 302, 1600553.
[43]. Farahani RD, Dubé M, Therriault D, Adv. Mater 2016, 28, 5794. [PubMed: 27135923]
[44]. Vyatskikh A, Kudo A, Delalande S, Greer JR, Mater. Today Commun 2018, 15, 288.
[45]. Cooperstein I, Shukrun E, Press O, Kamyshny A, Magdassi S, ACS Appl. Mater. Interfaces, 2018, 10, 18879. [PubMed: 29741081]
[46]. Guo L, Xia H, Fan HT, Zhang YL, Chen QD, Zhang T, Sun HB, Opt. Lett 2010, 35, 1695. [PubMed: 20479853]
[47]. Passinger S, Saifullah MS, Reinhardt C, Subramanian KR, Chichkov BN, Welland ME, Adv. Mater 2007, 19, 1218.
[48]. Tynell T, Karppinen M, Semicond. Sci. Technol 2014, 29, 043001.
[49]. Tohver V, Morissette SL, Lewis JA, Tuttle BA, Voigt JA, Dimos DB, J. Am. Ceram. Soc 2002, 85, 123.
[50]. Araki S, Ishikawa Y, Wang X, Uenuma M, Cho D, Jeon S, Uraoka Y, Nanoscale Res. Lett 2017, 12, 419. [PubMed: 28629209]
[51]. Liu Z, Fan T, Ding J, Zhang D, Guo Q, Ogawa H, Ceram. Int 2008, 34, 69.
[52]. Giakoumaki AN, Kenanakis G, Klini A, Androulidaki M, Viskadourakis Z, Farsari M, Selimis A, Sci. Rep 2017, 7, 2100. [PubMed: 28522845]
[53]. Bagal A, Zhang XA, Shahrin R, Dandley EC, Zhao J, Poblete FR, Oldham CJ, Zhu Y, Parsons GN, Bobko C, Chang CH, Sci. Rep 2017, 7, 9145. [PubMed: 28831168]
[54]. Fonseca RD, Correa DS, Paris EC, Tribuzi V, Dev A, Voss T, Aoki PH, Constantino CJ, Mendonca CR, J. Polym. Sci., Part B: Polym. Phys 2014, 52, 333.

[55]. Bael MKV, Hardy A, Mullens J, in Chemical Solution Deposition of Functional Oxide Thin Films, (Eds: Schneller T, Waser R, Kosec M, Payne D), Springer-Verlag, Wien, Austria, 2013, pp. 93–140.

[56]. Danks A, Hall S, Schnepp Z, Mater. Horizons 2016, 3, 91.

[57]. Varma A, Mukasyan AS, Rogachev AS, Manukyan KV, Chem. Rev 2016, 116, 14493. [PubMed: 27610827]

[58]. Hwang C-C, Wu T-Y, Mater. Sci. Eng. B 2004, 111, 197.

[59]. Leonard DN, Chandler GW, Seraphin S, in Characterization of Materials, (Eds: Kaufmann EN), John Wiley & Sons, Inc, New York, USA, 2012, pp. 1721–1735.

[60]. Peschot A, Qian C, Liu T-J, Micromachines 2015, 6, 1046.

[61]. Zaghloul U, Piazza G, in IEEE 26th International Conference on Micro Electro Mechanical Systems (MEMS), IEEE, 2013, pp. 233–236.

[62]. Machado MB, Sawan M, Schneider MC, Galup-Montoro C, in Proceedings of the 27th symposium on integrated circuits and systems design. ACM, 2014, pp. 25.

[63]. Chen K, Chen Y, Wei W, in 2017 IEEE/SICE International Symposium on System Integration (SII), IEEE, 2017, pp. 115–120.

[64]. Cui H, Hensleigh R, Yao D, Maurya D, Kumar P, Kang MG, Priya S, Zheng XR, Nat Mater. 2019, 18, 234. [PubMed: 30664695]

[65]. Shu L, Liang R, Yu Y, Tian T, Rao Z, Wang Y, J. Mater. Chem. C 2019, 7, 2758.

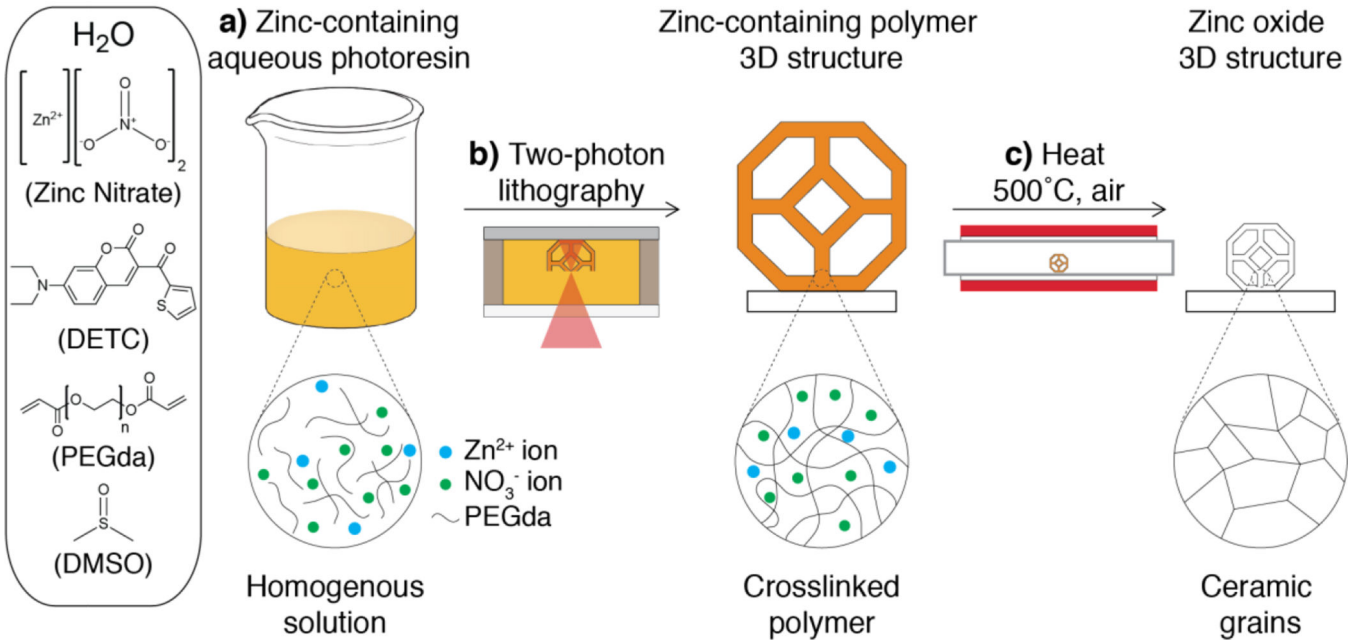

Figure 1.

Step-by-step synthesis route for additive manufacturing of micro- and nano-architected metal oxides. a) A zinc-ion containing aqueous photoresin is prepared by mixing zinc nitrate, water, PEGda, DETC, and DMSO to create a homogeneous pale orange solution. b) Two-photon lithography (TPL) is used to selectively pattern the zinc-ion containing photoresin into the designed 3D architecture. c) Calcination at 500°C produces a zinc oxide replica of this 3D structure with isotropic linear shrinkage. The shrinkage observed could be tuned by the initial metal salt loading and the development time of the structure in water.

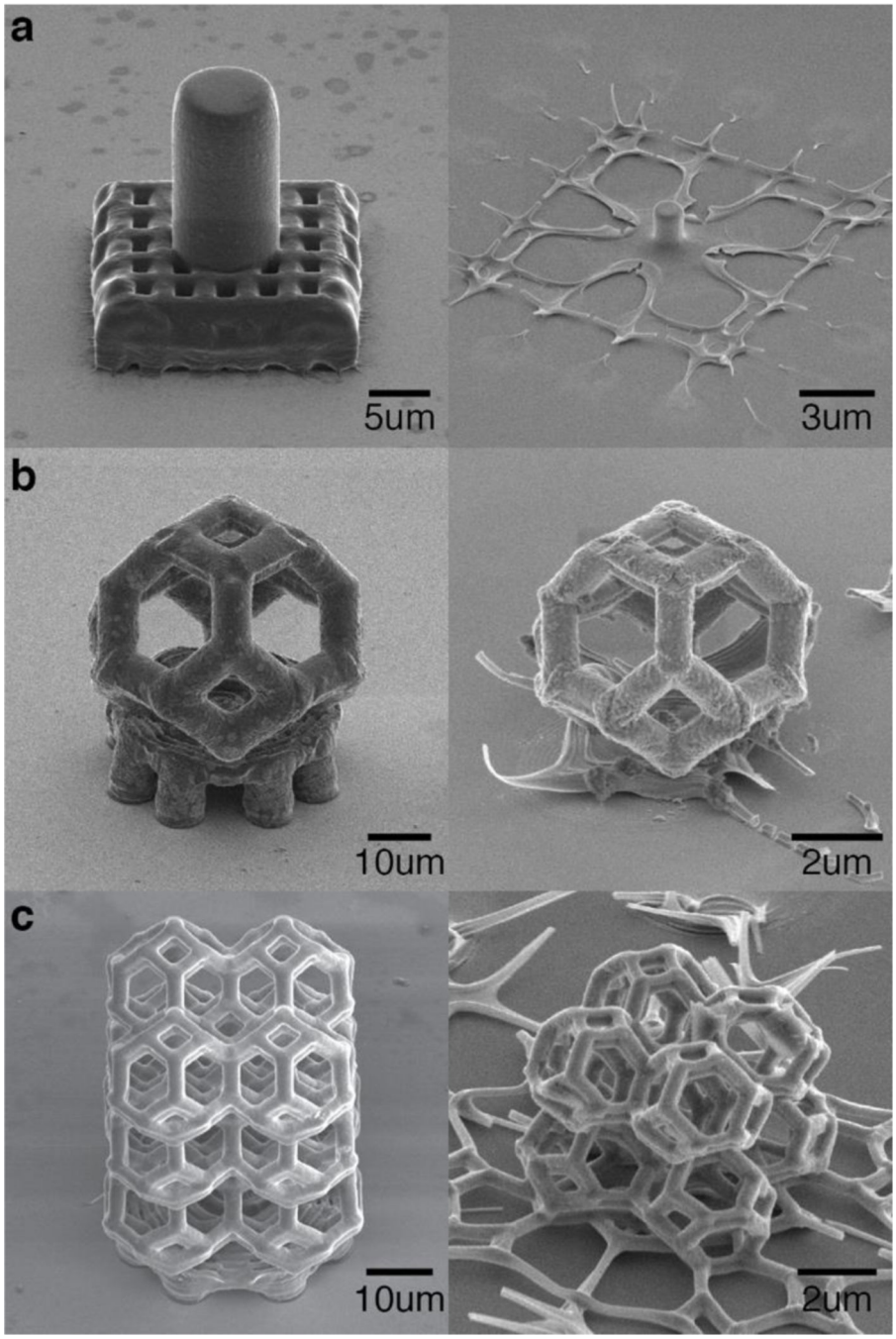

Figure 2.

Scanning electron microscopy (SEM) images of a) a cylindrical pillar, b) a tetrakaidecahedron unit cell, and c) a microlattice of tetrakaidecahedrons made via TPL of the aqueous Zn-ion photoresin before (left) and after (right) calcination. The linear dimensions of all structures were reduced by 87 ± 2 %.

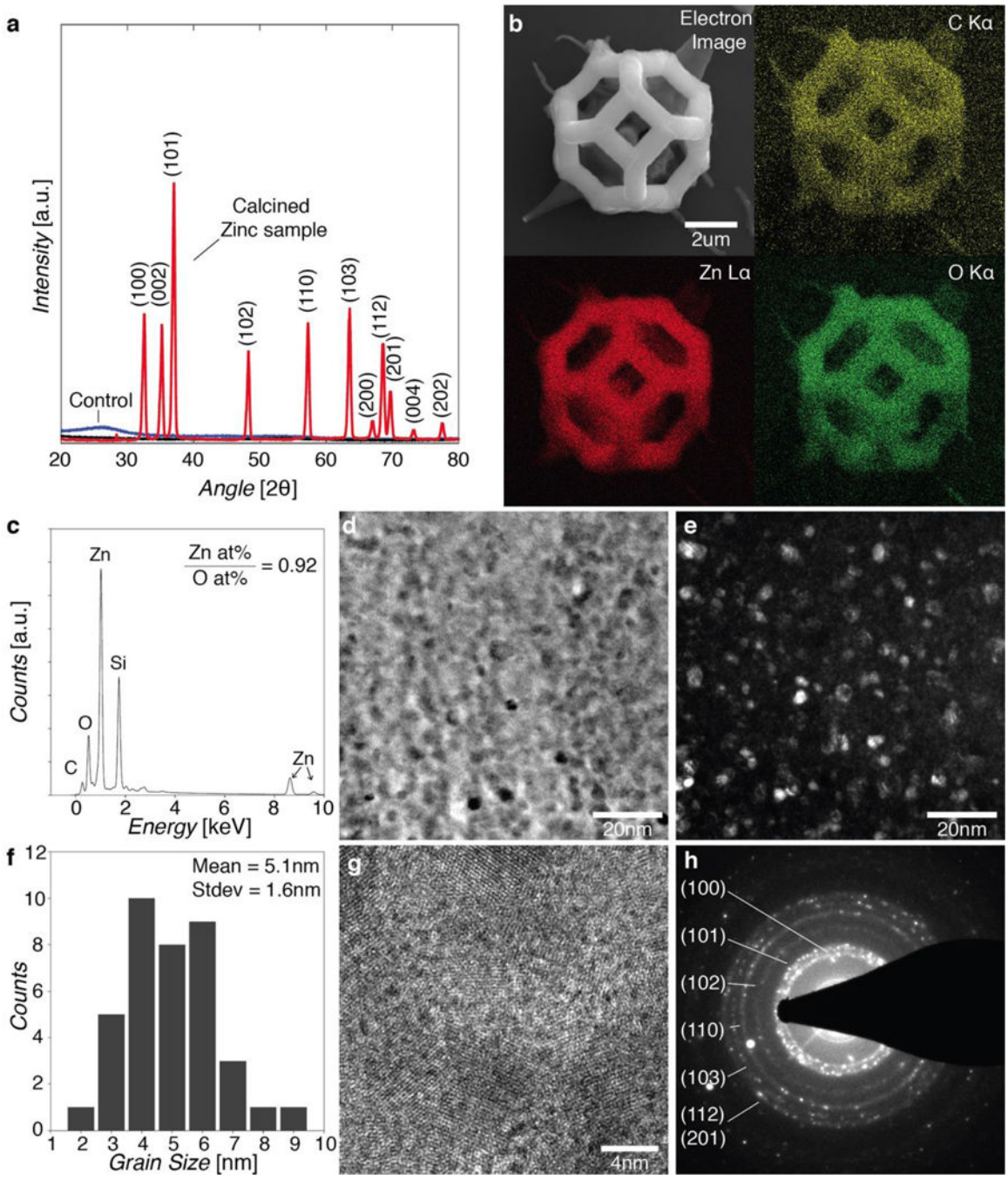

Figure 3.

Characterization of architected ZnO. a) XRD spectra of polymers with (red, diffraction peaks) and without (blue) the zinc precursor after calcination. b) Zinc, carbon and oxygen EDS maps of a tetrakaidecahedron unit cell after calcination. c) EDS spectrum obtained from a beam of the structure. Atomic ratio of Zn to O is ~0.92. d) Bright field, e) dark field, and g) high-resolution TEM images, and h) a TEM diffraction pattern taken from the cross-section of a calcined 3D ZnO structure all reveal nanocrystalline microstructure. f)

Histogram of grain sizes measured from the dark field TEM image revealed that they were 5.1 ± 1.6 nm in diameter (N=40).

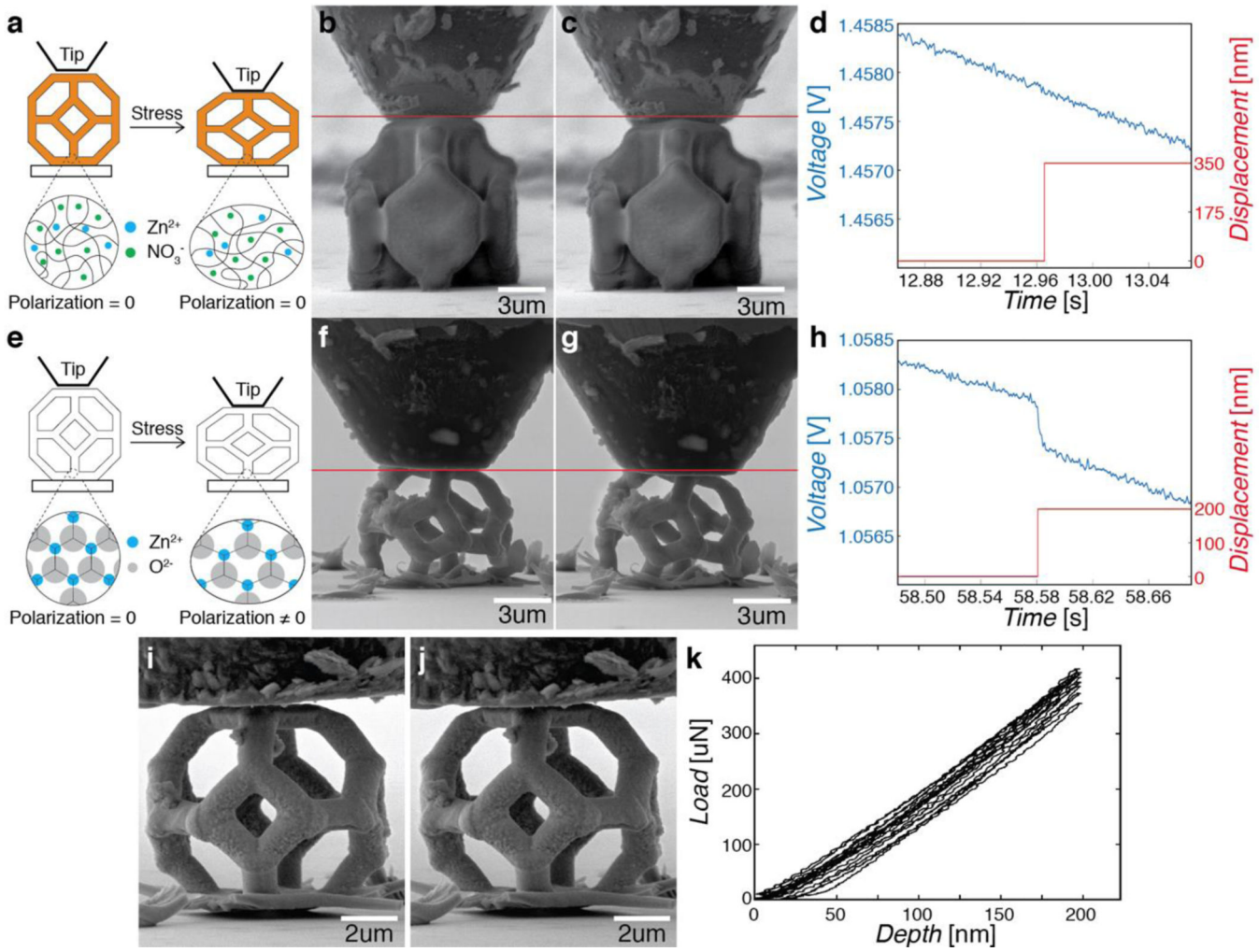

Figure 4.

Electromechanical response of 3D-architected ZnO. a) A schematic of in-situ mechanical compression of a zinc-ion containing tetrakaidecahedron polymer structure. The strain depicted is exaggerated for illustration. No net polarization is expected before and after compression because the polymer is not electromechanically active. SEM images during a typical in-situ experiment b) prior to compression and c) at approximately 350 nm of linear displacement. The red line serves as a guide to the eye (Figure S8 contains a magnified image of the compressions). d) Open circuit voltage (OCV) data depicts no measurable deviation of voltage from baseline system behavior. e) Schematic of compression of a ZnO tetrakaidecahedron structure, whose anisotropic crystal structure causes net polarization under strain. The strain depicted is exaggerated for illustration. SEM images during an in-situ experiment f) prior to compression and g) after approximately 200 nm of displacement. h) OCV data depicts a 0.52 mV voltage drop after a displacement of 200 nm at t = 58.58s. i) SEM images of the ZnO structure before and j) after 9 cycles of uniaxial compression of 200 nm. k) Load-displacement curves of the structure during cyclic loading showed no

significant deviation from elastic behavior. The slight displacement shifts observed were likely due to drift within the mechanical experiment.